Check for updates

Aluminium MOF as a selective sensor for atrazine with docking and computational insight

Simranjeet Singh, [ID][a] Radhika Varshney,† Pavithra N.,†[a] Basavaraju Uppara,[bc] Praveen C. Ramamurthy [ID] *[ab] and Nabila Shehata [ID][de]

An aluminium-based metal–organic framework (Al-MOF), constructed using 2,6-naphthalenedicarboxylic acid (2,6-NDC) as a linker, was synthesized for the selective electrochemical detection of atrazine (ATZ) in water. This study explores the molecular interactions between the Al-MOF and ATZ, supported by docking simulations and quantum chemical calculations, which reveal a strong binding affinity and electronic interaction. The sensor electrode modified with Al-MOF exhibited prominent enhancement in the peak current responses for ATZ compared to the bare carbon paste electrode, attributed to improved sensitivity and selectivity. Its performance was consistent across diverse water samples, with reproducibility demonstrated over multiple fabricated electrodes. Optimal detection was achieved using 0.1 M HCl as the supporting electrolyte, while interference studies confirmed a selective response for ATZ over other pesticides. The analysis revealed that the detection process is predominantly adsorption-controlled, and the method proved viable for real-world monitoring in drinking water and wastewater. Structural, compositional, and morphological characterization validated the integrity and stability of the synthesized Al-MOF. The overall findings highlight the practical utility of the Al-MOF-based sensing platform as an affordable and reliable approach for the environmental monitoring of persistent herbicides such as ATZ.

1 Introduction

Herbicides are a mixture of various organic compounds used to mitigate, destroy, or prevent pests.[1] Extensive use of herbicides in the last few decades has raised serious environmental concerns.[2] The carcinogenic and cytotoxic behaviour of herbicides results in respiratory, neurological, and infertility disorders.[1,3] Even when herbicides are applied over a limited area, they can spread far beyond their original location by becoming airborne, leaching into the soil, or dissolving in water and traveling through aquatic systems.[1,4] Atrazine (ATZ), a compound classified as 1-chloro-3-ethylamino-5-isopropylamino-*s*-triazine, has been widely utilized since its introduction in 1958 as an effective herbicidal agent against dicotyledonous plants, making it the most extensively applied

pesticide within the chloro-triazine group due to its remarkable efficiency.[5] Despite being prohibited in certain nations over concerns regarding its safety, ATZ continues to leave behind some of the most persistent and concentrated residues in environmental sources like groundwater when compared to other herbicidal compounds.[6,7] Concentrations of ATZ in rivers and surface waters frequently exceed established environmental thresholds, ranging anywhere from 0.1 to 180 µg L^{-1}, raising serious concerns not only for aquatic life but also for human health due to its tendency to bioaccumulate.[8] Atrazine has been linked to a range of harmful biological impacts, such as alterations in physical structure, hormonal imbalance, and changes at the molecular level, which can contribute to serious health conditions, including cancer, metabolic dysfunctions, and neurological disorders.[9–11]

Regular monitoring of ATZ by different organizations has consistently detected ATZ residues in aquatic environments, particularly in regions dominated by agricultural activity, underscoring its long-lasting presence.[12] This persistent contamination stresses the urgent need for effective removal and sensitive detection strategies to minimize exposure hazards and protect both environmental and public health. A variety of methods, including high-performance liquid chromatography, gas chromatography, and capillary zone electrophoresis, have been employed to identify ATZ that interferes with photosynthesis.[13] While these techniques offer excellent sensitivity, they are often limited by high operational costs, lengthy processing

[a] Interdisciplinary Centre for Water Research (ICWaR), Indian Institute of Science, Bengaluru, Karnataka 560012, India. E-mail: praveen@iisc.ac.in

[b] Department of Materials Engineering, Indian Institute of Science, Bengaluru, Karnataka 560012, India

[c] Centre for Smart Manufacturing Precision Machine Tools & Aggregates (C-SMPM), Central Manufacturing Technology Institute (CMTI), Bengaluru, Karnataka 560022, India

[d] Environmental Science and Industrial Development Department, Faculty of Postgraduate Studies for Advanced Sciences, Beni-Suef University, Egypt

[e] Renewable Energy Department, Korean Egyptian Faculty for Industry and Energy Technology, Beni-Suef Technological University, Egypt

† Equal contribution.

times, complex sample preparation steps, and challenges related to portability and on-site application. In this context, sensor technologies serve as a promising adjunct to conventional analytical methodologies by facilitating cost-effective, real-time, and on-site detection of environmental contaminants, thereby advancing the efficiency and resolution of environmental surveillance. Among various sensing platforms, electrochemical sensors have exhibited notable efficacy in achieving high sensitivity and selectivity at a reduced cost, even when applied to complex and heterogeneous sample matrices.

In recent years, metal–organic frameworks (MOFs) have attracted significant scientific attention due to their exceptionally large surface areas, customizable architectures, notable luminescent behaviour, and favourable electrochemical characteristics.[14] Aluminium-based metal–organic frameworks (Al-MOF) represent a highly tunable class of porous crystalline materials that have attracted considerable research interest in recent years due to their structural diversity and multifunctional properties.[15] These frameworks are typically constructed through the coordination of trivalent aluminium ions with organic dicarboxylate ligands under regulated thermal and pressure conditions, resulting in extended three-dimensional architectures.[16] Their inherent attributes, such as high surface area, thermal and chemical stability, and customizable pore

environments, render them suitable for diverse applications, including gas adsorption and separation processes, analyte sensing, heterogeneous catalysis, targeted pharmaceutical delivery, and environmental decontamination strategies. Comprehensive evaluations of Al-MOFs encompassing synthetic methodologies, physicochemical behavior, and functional deployment have been reported by Samokhvalov et al..[17] More recent advances, including innovations in material design and application breadth, have been detailed in the review by Fan et al..[15] These studies highlight the expanding role of Al-MOFs in various scientific domains.

In the present work, Al-MOF was synthesized via the coordination of organic linker 2,6-naphthalenedicarboxylic acid (2,6-NDC) with aluminium ions. The characteristics of the resulting framework were systematically investigated for its potential application in detecting ATZ in aqueous media. To evaluate real-world applicability, the sensing performance of the synthesized Al-MOF in detecting ATZ was further validated in real samples.

2 Materials & synthesis

2.1 Chemicals and reagents

All chemicals used in this work were of analytical grade and employed without any further purification. $Al(NO_3)_3 \cdot 9H_2O$,
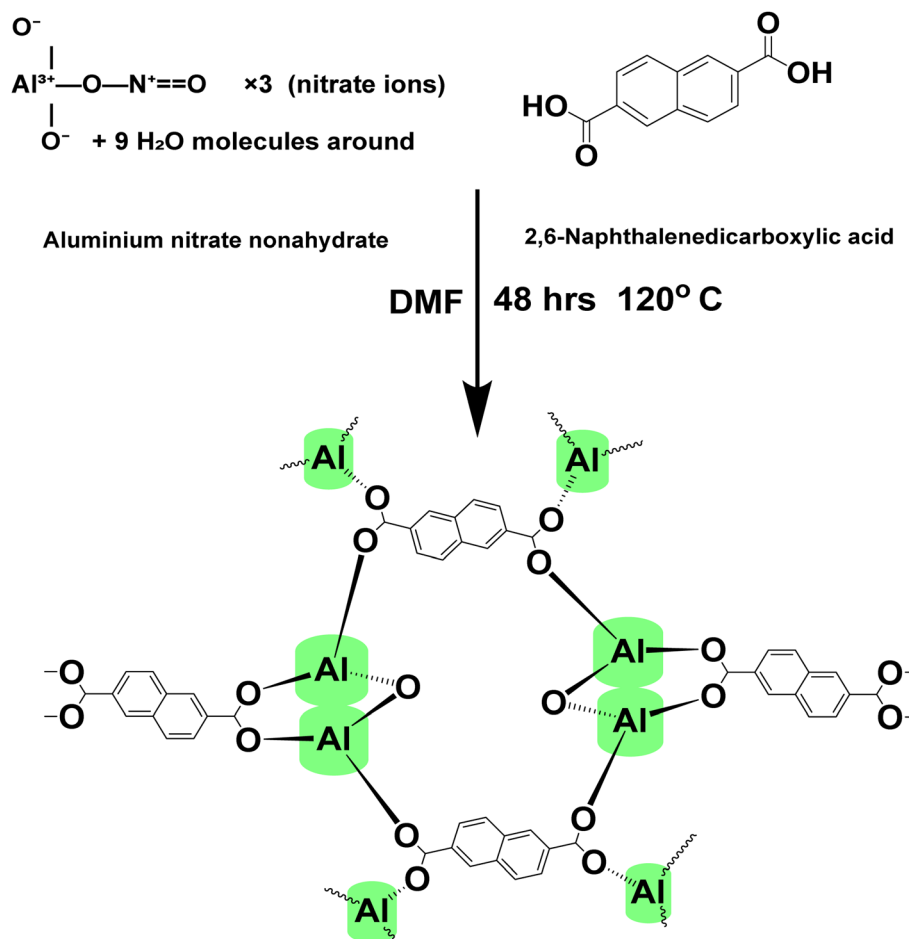
Scheme 1 Step-by-step synthesis mechanism of AL-MOF.

ATZ, dimethylformamide (DMF), and 2,6-NDC were obtained from Sigma-Aldrich, Bengaluru, India. Standard solutions of ATZ and other pesticides were prepared by dissolving appropriate amounts in MilliQ water, which had a conductivity of 5.8 dS m^{-1}.

2.2 Preparation of Al-MOF

Aluminium-based MOF was synthesized *via* a solvothermal process, adapted from the protocol used in our previous study[18] with slight modifications. In a typical procedure, 3 g of aluminium nitrate nonahydrate and 1 g of 2,6-NDC were added to 100 mL of DMF and mixed thoroughly. The resulting solution was transferred to a stainless-steel autoclave lined with Teflon and heated at 120 °C for 48 h. Upon cooling, a pale white solid was formed, which was isolated by centrifugation and washed several times with DMF and ethanol to eliminate any unreacted residues. The product was then dried in a vacuum oven at 60 ± 5 °C for 12 h. The resulting fine powder was labelled as Al-MOF. The scheme for the synthesis of Al-MOF is represented below (Scheme 1).

2.3 Docking studies and computational methodology

Molecular docking simulations were carried out to investigate the potential interactions between Al-MOF and ATZ. A prototype structure of Al-MOF was constructed using ChemDraw (v22.0.0) and subjected to geometry optimization *via* the Forcite module within the Materials Studio. The optimized structure was then exported in Protein Data Bank (PDB) format. The 3D structure of ATZ (PubChem CID: 2256) was obtained from the PubChem database in SDF format and subsequently optimized using the default parameters in Avogadro. The resulting structure was saved in PDB format for further analysis and interpretation. In the docking workflow, Al-MOF was designated as the macromolecule, and ATZ as the ligand. Blind docking was performed using Auto Dock Tools (ADT). A grid box of dimensions $100 \times 60 \times 72$ points with a spacing of 0.36 Å was defined for the autogrid4 calculations. Molecular docking was executed using Autodock4 with the Lamarckian genetic algorithm, employing a population size of 300 and 500 independent runs. The resulting binding poses were ranked based on binding energy, and the top-ranked conformation was selected for further visualization and interaction analysis using Discovery Studio Visualizer (DSV). All quantum chemical calculations were carried out using the DMol3 module within the BIOVIA Materials Studio. The frontier molecular orbitals of the Al-MOF complex and its interaction with ATZ were investigated. Geometry optimization of the isolated Al-MOF and the Al-MOF–ATZ complex was initially performed using the Forcite module.

2.4 Electrochemical detection

Electrochemical experiments were performed using a three-electrode system comprising Ag/AgCl as the reference electrode, a platinum wire as the counter electrode, and a carbon paste electrode (CPE) as the working electrode. The bare carbon paste electrode (BCPE) was prepared by homogenizing 0.24 g of graphite powder with 40 μL of silicone oil. The paste was packed

into the electrode cavity, polished to obtain a smooth surface, and electrically connected to a PalmSens4 electrochemical workstation using a conducting wire. The modified carbon paste electrode (MCPE) was fabricated by uniformly mixing 12 mg of synthesized Al-MOF composite with 0.228 g of graphite powder and 40 μL of silicone oil. The resulting MCPE was assembled following the same procedure as the BCPE. The EIS experiments were carried out in the frequency range of 5 Hz to 50 kHz. CV measurements were recorded over an appropriate potential window at a scan rate of 50 mV s^{-1} from −0.2 to 0.8 V. All measurements were performed at room temperature in the supporting electrolyte under optimized experimental conditions.

2.4.1 Influence of the Al-MOF modified working electrode on ATZ detection. The performance of the Al-MOF modified carbon paste working electrode (Al-MOF/MCPE) incorporating Al-MOF was explored by comparing it with the BCPE. In a typical experiment, a blank DPV run is conducted in 0.1 M HCl (24 mL) as a supporting electrolyte, followed by the addition of ATZ (120 μL from a 10 mM stock solution) and the recording of a DPV run.

2.4.2 Influence of supporting electrolyte on ATZ sensing. The influence of various supporting electrolytes, including NaOH (pH ∼ 13), HCl (pH ∼ 1), phosphate buffer (PBS, pH ∼ 7), and acetate buffer (pH ∼ 5), at a concentration of 0.1 M each, has been investigated. In a typical experiment, a blank DPV run is conducted in a particular supporting electrolyte, followed by the addition of ATZ (120 μL from a 10 mM stock solution) and the recording of a DPV run.

2.4.3 Stability and reproducibility. The stability of the Al-MOF/MCPE has been estimated using the cyclic voltametric technique by performing multiple CV cycles in the presence of 240 μL ATZ (10 mM stock solution). The reproducibility of the Al-MOF/MCPE has been evaluated by fabricating four distinct working electrodes and using them for ATZ detection. In a typical experiment, a blank DPV run is conducted in 0.1 M HCl as the supporting electrolyte, followed by the addition of ATZ (120 μL from a 10 mM stock solution) and the recording of a DPV run.

2.4.4 Selectivity and interference. The selectivity of the Al-MOF/MCPE has been investigated by considering its application for the detection of a fixed quantity (120 μL from a 10 mM stock solution) of other pesticides, such as tebuconazole (Teb), imidacloprid (Imi), cypermethrin (Cyper), and cyanuric acid (CA). Whereas the interference studies were conducted to detect ATZ (120 μL from a 10 mM stock solution) in the presence of other pesticides individually (120 μL from a 10 mM stock solution). The supporting electrolyte was 0.1 M HCl.

2.4.5 Influence of concentration variation and LOD determination. The influence of changing the concentration of ATZ was investigated using the standard addition method, which involves the incremental addition of ATZ in the same electrochemical cell and recording the DPV run after each addition. Herein, 30 μL from the 10 mM ATZ stock solution was added repeatedly after recording each DPV run, in 24 mL of 0.1 M HCl.

2.4.6 Mechanism of electrochemical detection. The mechanism of electrochemical detection, whether adsorption-

controlled or diffusion-controlled, can be deduced by analysing the variation of scan rate using cyclic voltammetry (CV). Herein, the scan rate has been varied from 10 mV s^{-1} to 100 mV s^{-1}, and the CV response has been recorded for the electrochemical cell containing 120 μL of ATZ (from a 10 mM stock solution) in the presence of 0.1 M HCl as the supporting electrolyte.

2.4.7 Real-world sample analysis. The utilization of Al-MOF/MCPE in the real-world sample analysis has been studied using deionized water, tap water, milk samples, and filtered sewage water. Prior to analysis, the tap samples were filtered to remove suspended solids and appropriately diluted with the supporting electrolyte to minimize matrix interference and ensure compatibility with the electrochemical system. Milk was diluted (1 : 10) with distilled water, centrifuged to remove fats and proteins, and the supernatant was filtered through a 0.45 μm membrane filter. The filtrate was mixed with the supporting electrolyte prior to analysis. Sewage water was allowed to settle and then sequentially filtered using Whatman No. 1 filter paper, followed by a 0.45 μm membrane filter. The filtered sample was diluted with the supporting electrolyte, if required, and used for electrochemical measurements.

3 Results & discussion

3.1 Docking findings

The top-ranked conformation obtained from molecular docking simulations exhibited a binding energy of −3.82 kcal mol^{-1}, with an estimated inhibition constant of 1.858 mM at 298 K.

The electrostatic contribution to the binding energy was positive (+0.25 kcal mol^{-1}), indicating that the interaction is primarily stabilized by non-electrostatic forces (Fig. 1). The negative overall binding energy suggests a thermodynamically favourable association between Al-MOF and ATZ. The calculated HOMO and LUMO energy levels of the pristine Al-MOF complex were −5.865 eV and −5.579 eV, respectively. Upon interaction with ATZ, a significant shift in the frontier molecular orbital energies was observed. The HOMO and LUMO energy levels of the Al-MOF–ATZ complex were found to be −0.1798 eV and −0.10425 eV, respectively. This substantial reduction in energy levels indicates a strong electronic interaction between the Al-MOF and ATZ.

3.2 Structural, functional, and elemental characterization of Al-MOF

3.2.1 FT-IR. The FTIR spectrum of Al-MOF (Fig. 2a) shows the characteristic peaks of Al-MOF as follows: sharp peak at 3687 cm^{-1}, broad peak at 3439 cm^{-1} and 995 cm^{-1} are referred to as O–H vibrations of the surface of isolated hydroxyl groups, and they may also refer to a trace amount of adsorbed water.[19] Additionally, it refers to stretching bands of OH, which originated from μ_2-hydroxo groups in AlO$_4$(OH)$_2$.[20,21] The absorption peaks at C–N (1263 cm^{-1}), C–O (1368 cm^{-1}), and C=O (1600 cm^{-1} and 1661 cm^{-1}) of DMF solvent as well as C=C (1431 cm^{-1} and 1518 cm^{-1}), and C–H of aromatic ring (1086 cm^{-1}) in MOF[22] confirming the integrity of the Al-MOF structure.[23] Three peaks at 748 cm^{-1}, 789 cm^{-1}, and 843 cm^{-1}
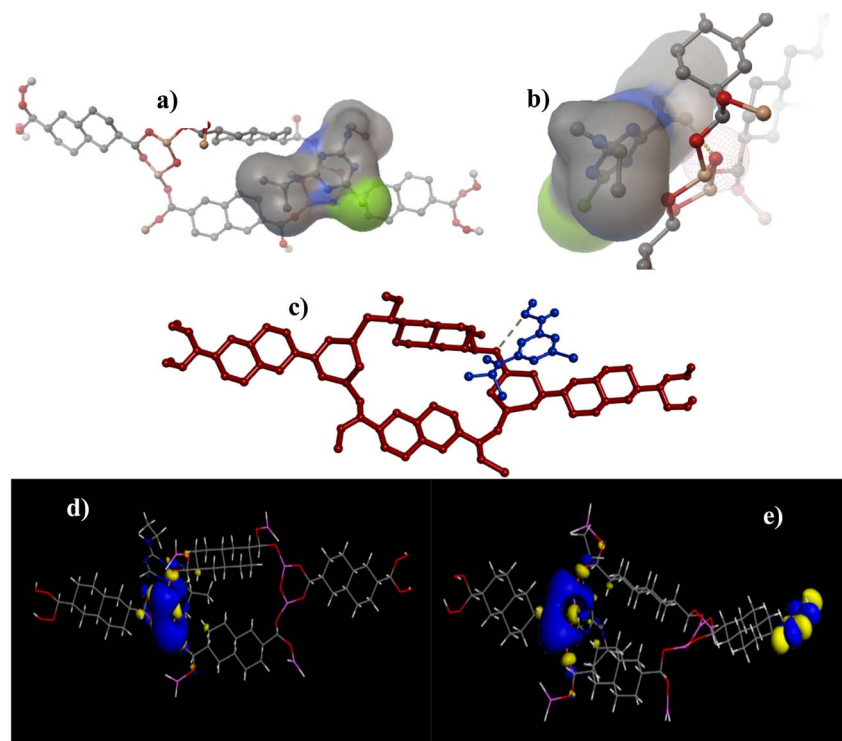

Fig. 1 Top-ranked docked conformation of the Al-MOF–ATZ complex as visualized using (a) ADT showing the overall binding orientation; (b) enlarged view highlighting key molecular interactions at the binding site; and (c) DSV representation (Al-MOF: red; ATZ: blue); Frontier molecular orbitals of Al-MOF with ATZ HOMO (d) and LUMO (e).
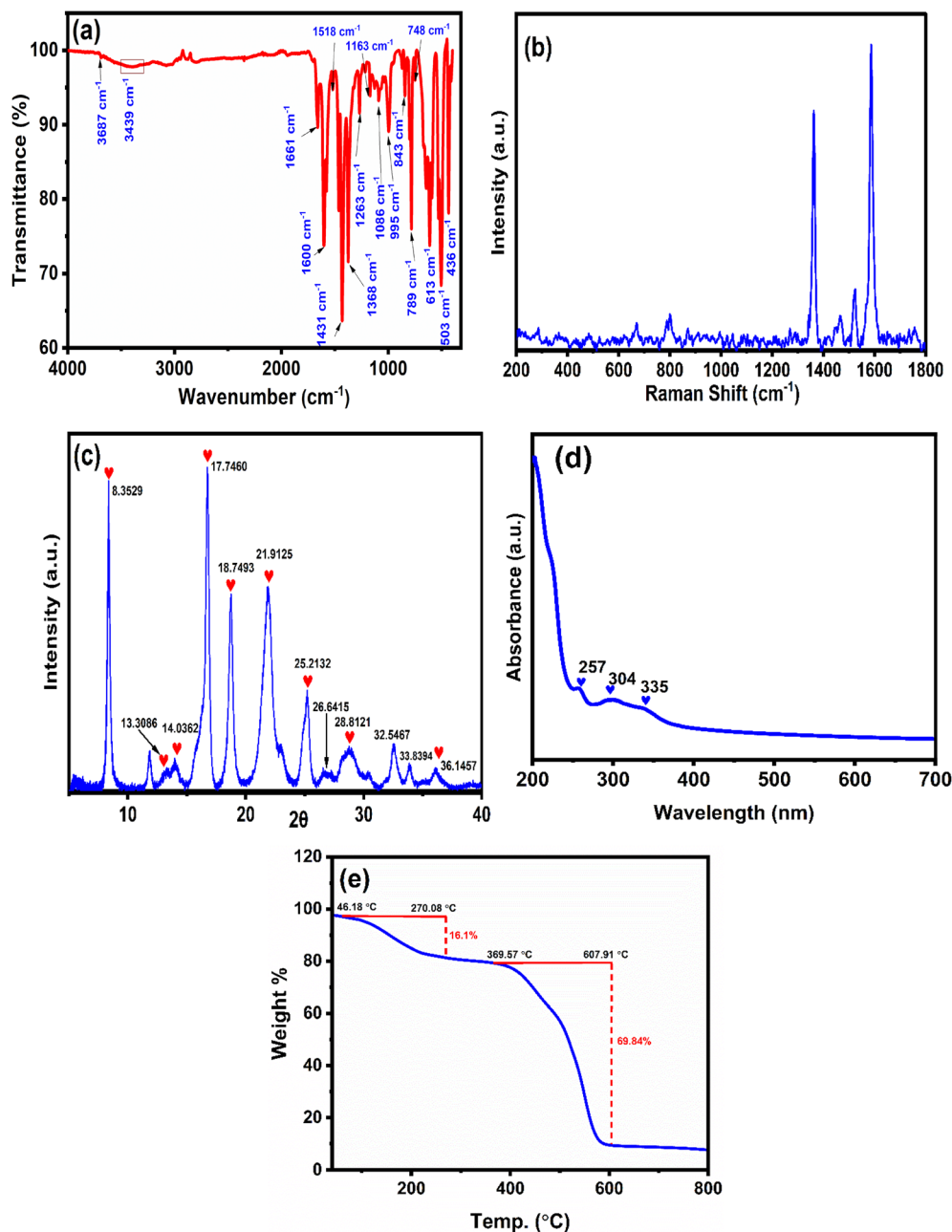
Fig. 2 (a) FTIR, (b) Raman, (c) XRD, (d) UV, and (e) TGA analyses of the developed Al-MOF.

are associated with aromatic C–H bending, further supporting the presence of the aromatic ligand in the framework.[24] The bands at 1163, 613, 503, and 436 cm^{-1} may be associated with the stretching vibrations of the Al atom with oxygen atoms (ν(Al–O)).[25–27]

3.2.2   Raman. To accomplish a more accurate view of the vibrational modes of Al-MOF, FT-IR spectroscopy was supported with Raman spectroscopy, as seen in Fig. 2b. The spectrum shows the characteristic peaks in the range of 1300–1600 cm^{-1}, which agrees with previous studies.[25,28] Two distinctive peaks appear at ~1361 and 1590 cm^{-1} attributed to in-plane ring deformation modes and stretching vibrations of MOF linker, respectively.[29]

3.2.3   XRD. The structures of the Al-MOF are further characterized by the XRD spectrum (Fig. 2c). Here, the as-developed Al-MOF shows the characteristic diffraction peaks at 88.35° (110), 17.74° (211), 18.75° (220), and 21.9° (202), which confirms the successful synthesis of the DUT-4 structure and agrees with previous studies.[30,31] The XRD patterns are consistent with the simulated ones (CCDC no. 181153).[32] Moreover, the development of broad peaks is attributed to the nanosized crystallites, which agrees with the SEM results.

3.2.4   UV. As displayed in Fig. 2d, Al-MOF exhibits two absorption bands in the UV region, peaking at 257 and 304 nm, indicating characteristic electronic transitions. The peak at 257 nm may be attributed to the π–π* and n–π* transitions of
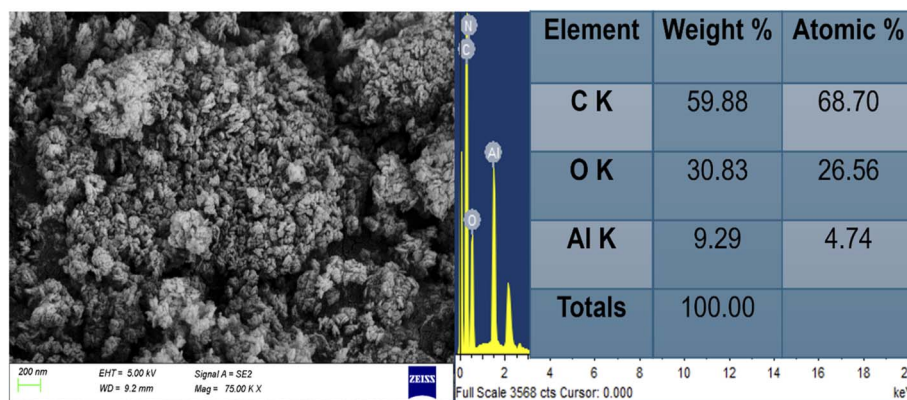
Fig. 3 SEM-EDX analysis of the Al-MOF.

the C=C and C=O groups, respectively. The broad peak at 304 nm with a shoulder at 335 nm could be attributed to the n– π* transition of C–OH or C=O groups of the Al-MOF.[33]

3.2.5 TGA. The thermogravimetric analysis of Al-MOF (Fig. 2e) showed that there is a weight loss 16.1% starting at 46.18 °C and ending at 270.08 °C. This weight loss is attributed to the evolution of H_2O and DMF. The major weight loss (69.84%) starts at 369.57 °C and ends at 607.91 °C. This weight loss was attributed to the deformation of Al-MOF because of dehydroxylation and transformation of Al-MOF to Al_2O_3.[30] According to the results, the developed Al-MOF is thermally stable up to 370 °C.

3.2.6 SEM-EDX. Fig. 3 shows that Al-MOF appears under the scanning electron microscope as particles with an oat-like shape, and they are agglomerated in large clusters in a disordered arrangement. The look of the particles is attributed to the multilayer nature of the MOF and the simultaneous process of nucleation and crystal growth. The EDX analysis indicates the presence of C, O, and Al, with % weight of 59.88, 30.83, and 9.29%, respectively.

3.2.7 XPS. XPS was used to analyze the elemental valence and surface chemical composition of Al-MOF. The XPS survey spectrum (Fig. 4a) shows the main elements of Al-MOF: C (284–289.22 eV), O (532.34 eV), Al (74.7 eV), and N (401.3 eV). The XPS spectrum of O 1s with a high-resolution (Fig. 4b) shows two deconvoluted peaks at binding energies of 530.9 eV, 532.34 eV, and 533.3 eV that can be attributed to Al–O, O–C=O, and Al–OH bonds, respectively. The high-resolution C 1s XPS spectrum (Fig. 4c) shows two distinctive peaks at binding energies 284.88 eV, and 289.22 eV. These correspond to C–C and O=C–O, respectively. The XPS spectrum of Al $2p_{3/2}$ is shown with a high resolution in Fig. 4d. The characteristic peak of Al $2p_{3/2}$ is located at a binding energy of 74.7 eV. The high-resolution N 1s spectrum (Fig. 4e) shows a peak at 401.3 eV refers to graphitic nitrogen.[34] However, the results confirm the successful development of Al-MOF and agree with previous studies.[35,36]

3.3 Electrochemical detection

The CV and EIS measurements of Al-MOF are presented in the supporting information (Fig. S1a and b, respectively).

3.3.1 Influence of the Al-MOF in the working electrode. The performance of the MCPE incorporating Al-MOF was explored by comparing it with the BCPE. The results obtained are depicted in Fig. 5a. The peak current obtained using MCPE is 3 times higher than the peak current obtained using BCPE for ATZ detection (*i.e.*, 9.5 μA for BCPE and 30.20 μA for MCPE). Therefore, it highlights the superior performance of MCPE over BCPE in detecting ATZ.

3.3.2 Influence of supporting electrolyte on ATZ sensing. The influence of the supporting electrolytes, such as NaOH (pH ∼ 13), HCl (pH ∼ 1), phosphate buffer (PBS, pH ∼ 7), and acetate buffer (ABS, pH ∼ 5), having concentrations of 0.1 M each, has been investigated (Fig. 5b). The maximum peak current is obtained in the presence of 0.1 M HCl as the supporting electrolyte, suggesting the efficacy of using 0.1 M HCl as the supporting electrolyte for ATZ detection utilizing Al-MOF/MCPE. Further, the absence of any peak in NaOH as a supporting electrolyte suggests that basic conditions are not favourable for ATZ detection, as ATZ may depict electroactive properties in acidic to near-neutral pH conditions.[37]

3.3.3 Stability and reproducibility. The stability of the Al-MOF/MCPE has been estimated using the cyclic voltametric technique (Fig. 6a). A gradual increase in the current response occurs as the number of CV cycles increases from 1 to 20, indicating an irreversible process and the system's inability to reach stability within 20 CV cycles. On the other hand, Fig. 6b, shows a well-defined redox peak around 0.3–0.4 V, indicating similar electrochemical behavior when taken after 6 h. A marginal decrease in current is observed after 6 h, suggesting a slight attenuation of electrochemical activity, likely due to surface stabilization or partial passivation of the electrode over time. The reproducibility of the Al-MOF/MCPE has been evaluated as shown in Fig. 6c. As observed, the standard deviation of the response (*i.e.*, current$_{ATZ}$ − current$_{blank}$) obtained at ∼0.35 V for ATZ sensing using four distinct electrodes is ∼2.5, indicating decent reproducibility.

3.3.4 Selectivity and interference. The absence of any potential interferences from other pesticides indicates the superior performance of the Al-MOF/MCPE in detecting ATZ (Fig. 7a). Additionally, the selectivity of the Al-MOF-modified
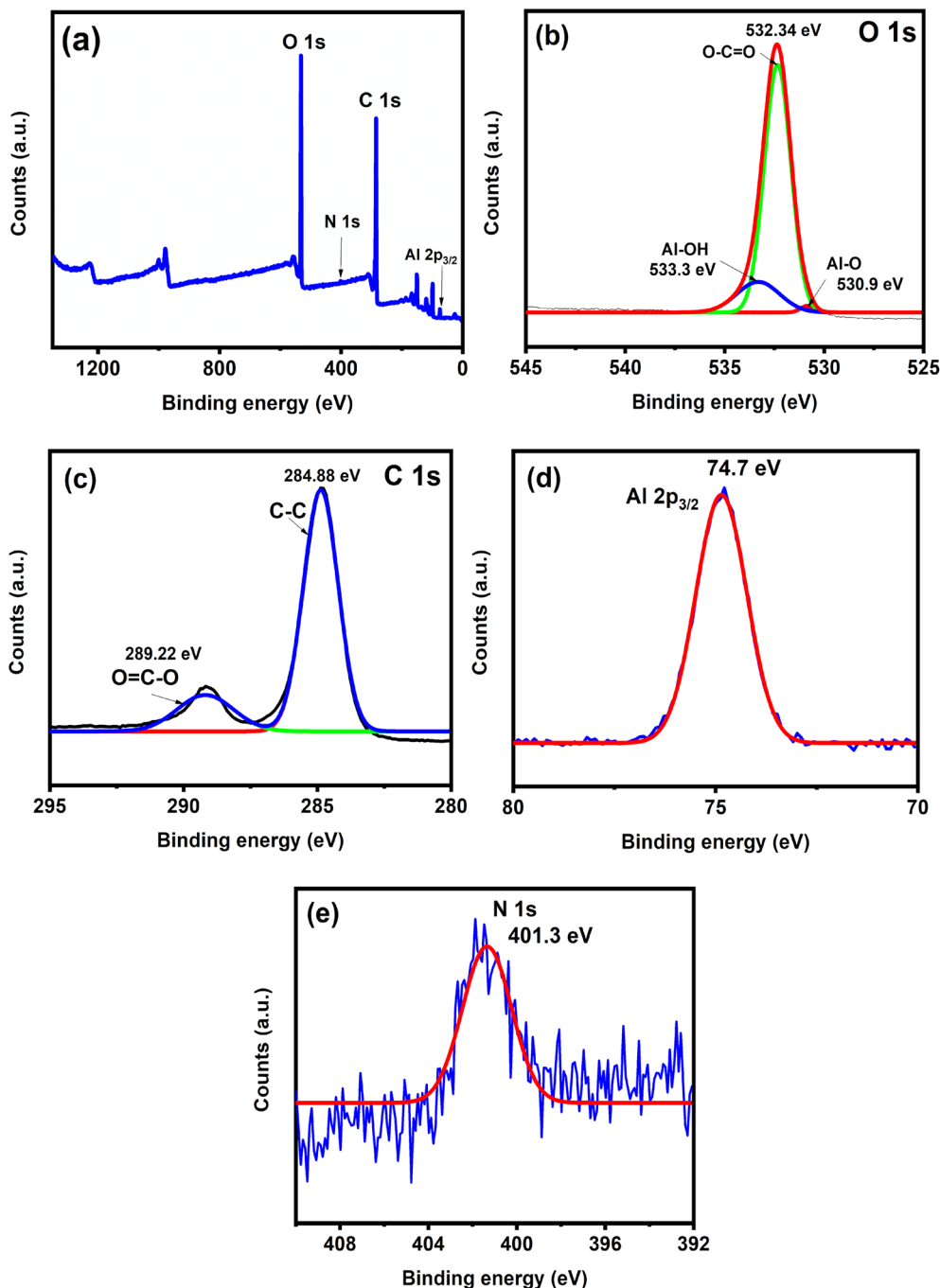
Fig. 4 XPS analysis of the Al-MOF (a), high resolution spectra of O 1s (b), C 1s (c), Al 2p$_{3/2}$ (d), and N 1s (e).

CPE is shown in Fig. 7b (a graph of peak current (ΔI_p) after subtracting from background *versus* interference in the inset), indicating that Al-MOF/MCPE is selective towards ATZ over the other pesticides considered.

3.3.5 Influence of concentration variation and LOD determination. The influence of varying the concentration of ATZ is illustrated in Fig. 8a, indicating that the peak current increases as the ATZ concentration is increased in the electrochemical cell. A linear relationship with an R^2 value of 0.99 has been established between the peak current and the ATZ concentration (Fig. 8b), as governed by eqn (1).

$$\text{Current signal (μA)} = 3.452 \times \text{concentration of ATZ (μM)} + 44.15 \quad (1)$$

$$\text{LOD} = 3\sigma/s \quad (2)$$

The limit of detection (LOD) is estimated using the IUPAC method (eqn (2)), wherein σ and s represent the standard deviation of 10 blank samples and the slope of the calibration curve, respectively. The standard deviation of ten independent blank samples is calculated to be 5.066 μA (Fig. S3). The LOD is
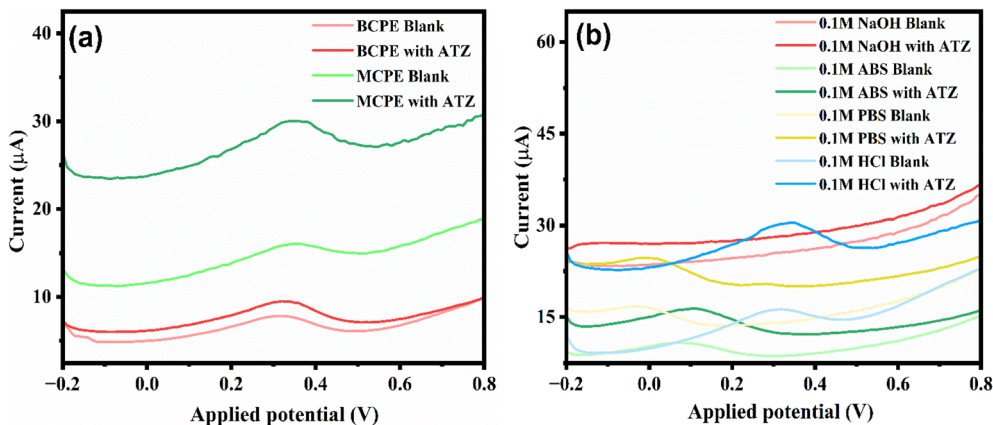
Paper

Fig. 5 DPV graphs of MCPE *vs.* BCPE for ATZ detection (a), and ATZ detection in various supporting electrolytes (b).

calculated to be 4.4 μM. Table 1 summarizes the comparison of the linear range and limits of detection (LOD) of various ATZ detection studies reported to date.

3.4 Mechanism of electrochemical detection

The mechanism of electrochemical detection, whether adsorption-controlled or diffusion-controlled, is investigated by analysing the variation of scan rate using cyclic voltammetry

(CV). The CV responses obtained are depicted in Fig. 8c. As the scan rate increases from 10 mV s^{-1} to 100 mV s^{-1}, the peak current response obtained also increases substantially (Fig. 8c). Also, the dependency of log peak current on log scan rate has been plotted (Fig. 8d). The existence of a linear relationship between the log peak current and log scan rate, with a value of slope ~1, indicates that the mechanism of electrochemical detection is adsorption controlled.
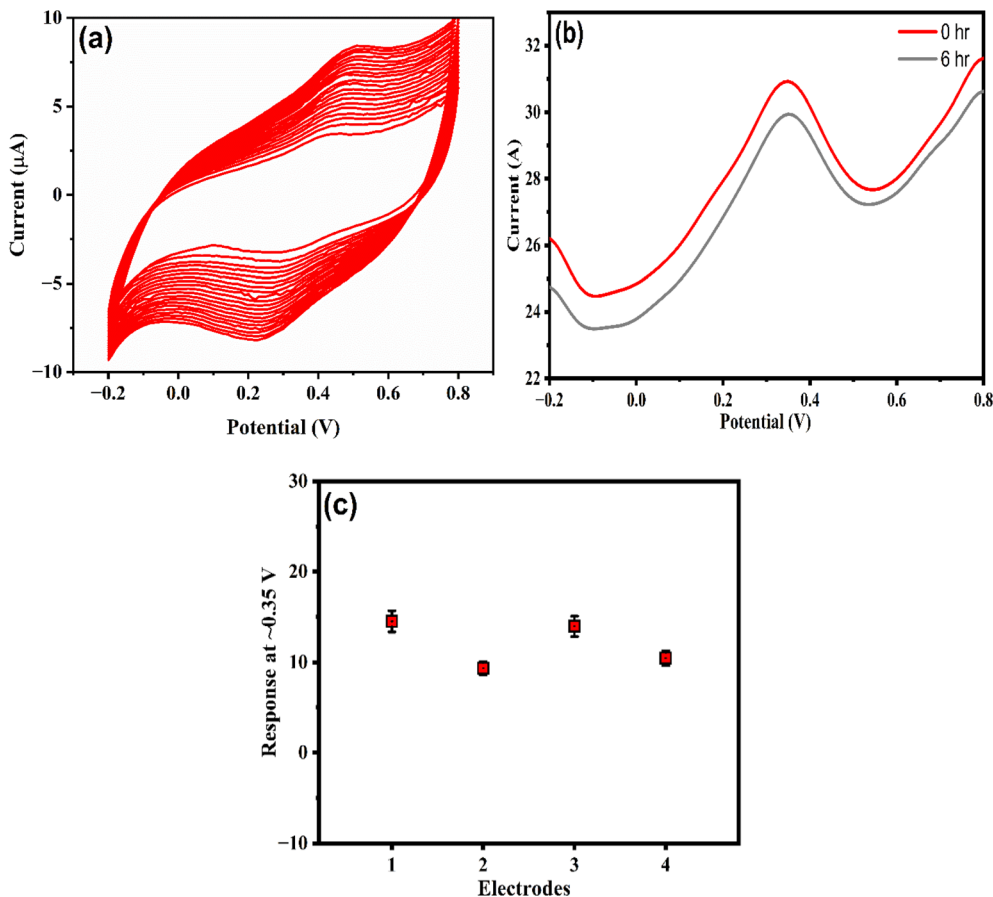

Fig. 6 (a) Stability graph of MCPE for ATZ detection, and (b) stability in terms of hours (c) reproducibility graph of ATZ detection using various fabricated electrodes.
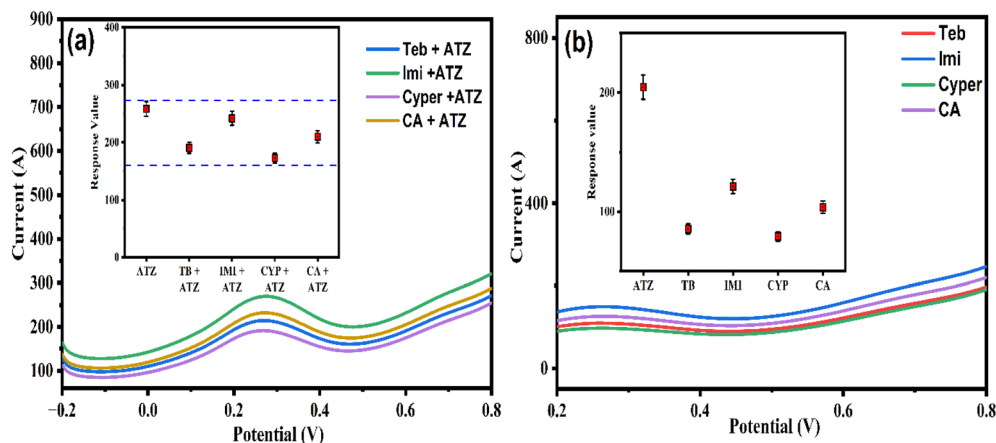
Fig. 7 (a) Interference graph of MCPE *vs.* BCPE for ATZ detection, and (b) selectivity studies of ATZ detection in various supporting electrolytes.

3.5 Real-world sample analysis

The utilization of Al-MOF/MCPE in the real-world sample analysis has been studied using deionized water, tap water, milk samples, and filtered sewage water. Eqn (1) has been utilized to estimate the concentration of ATZ in real samples based on the peak current signal obtained (Fig. S3). Table 2 presents the

results of real sample analysis, indicating the real-time performance of Al-MOF/MCPE. The relatively low detection efficiency (~94% to 88%) observed for ATZ in tap and sewage water samples can be due to the presence of coexisting ions, organic matter, and suspended particles in tap and sewage water, which may interfere with the electrochemical response of ATZ at the Al-MOF/MCPE surface. Additionally, the adsorption of these
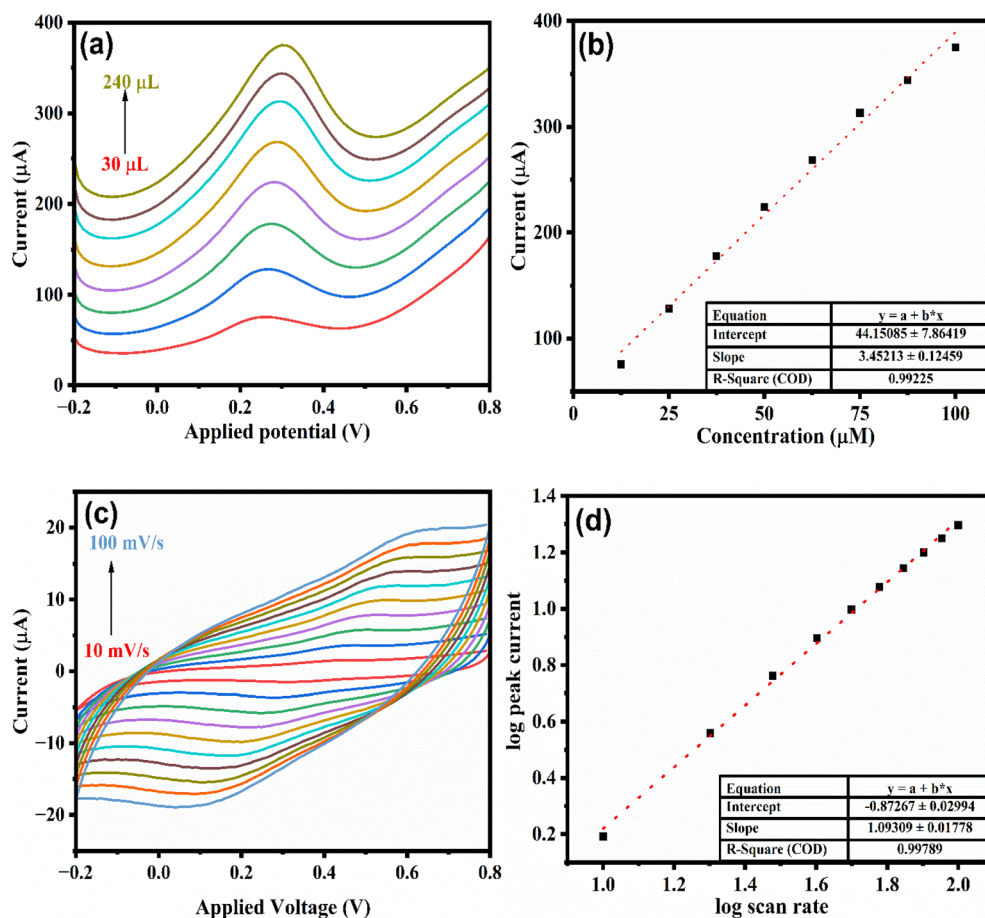

Fig. 8 (a) ATZ concentration variation in the DPV method, and (b) calibration curve between peak current and ATZ concentration, (c) CV graph for scan rate variation, and (d) log–log graph for mechanism prediction.

Table 1 A comparison table for the detection of ATZ

Sensor material	Linear range (μM)	LOD (μM)	Reference
Ha006a-modified multi-carbon paste electrode	10–100	5.4	38
Gold nanoparticles	10–30	10.9	39
Cell-free biosensor (enzyme or biomolecule-based sensing without intact cells)	—	20	40
Tyrosinase immobilized on polyvinyl alcohol/styryl-pyridinium polymer matrix	10–100	1.3	41
Zinc methylimidazolate framework (ZIF-type MOF)	10–100	1.73	42
Silica-coated atrazine molecularly imprinted polymer nanoparticles	—	1.8	43
Zeolitic imidazolate framework-67 modified multi-carbon paste electrode	10–100	3.7	13
Zinc oxide nanoparticles synthesized *via* green (biological/eco-friendly) methods	0.5–3	0.41	44
Silver nanoparticles	10–30	3.5	39
Al-MOF/MCPE	12.5–100	4.4	Present work

Table 2 Real sample analysis of Al-MOF/MCPE

Samples	Spiked (μL)	Detected (μM)	Efficiency (%)
Deionized water	5	4.95 ± 0.18	99%
	10	9.89 ± 0.32	98.9%
	15	14.81 ± 0.47	98.7%
	20	19.77 ± 0.63	98.9%
Milk samples	5	4.86 ± 0.21	97.2%
	10	9.81 ± 0.35	98.1%
	15	14.68 ± 0.54	97.9%
	20	19.42 ± 0.68	97.1%
Tap water	5	4.62 ± 0.22	92.4%
	10	9.33 ± 0.37	93.3%
	15	13.95 ± 0.59	93.0%
	20	18.92 ± 0.77	94.6%
Sewage water	5	4.45 ± 0.13	89.0%
	10	8.99 ± 0.24	89.9%
	15	13.48 ± 0.49	89.9%
	20	17.81 ± 0.44	89.1%

impurities onto the electrode surface may partially block the active sites, reducing electron transfer efficiency. Furthermore, sample pre-treatment or filtration might not completely remove interfering substances, leading to signal suppression and decreased recovery rates.

4 Conclusion

This work demonstrates that the Al-MOF can be useful for sensing ATZ in water. The material was carefully crafted and tested for its structure and stability before assessing how well it binds with ATZ molecules. Computer simulations, along with lab tests, showed that the framework interacts strongly with ATZ, which helps detect it effectively. When incorporated into an electrode, this MOF greatly improved the sensor's sensitivity compared to one without it. The sensor performed well under various conditions and with different types of real water samples, including tap water and wastewater. It also maintained consistent results across multiple tests, demonstrating its reliability for repeated use. Acidic conditions were found to be best for sensing ATZ using the developed material, and even in the presence of other pesticides, the sensor was selective for ATZ. The detection method primarily relies on adsorption,

where ATZ molecules adhere to the sensor surface, as confirmed by experiments conducted at varying scan rates. The detection limit was low enough to be useful for environmental monitoring. Overall, this sensor offers a simple, efficient, and cost-effective tool that could help monitor harmful herbicides in the environment. With further development, it may be possible to utilize this MOF in portable devices for field testing. This study contributes valuable knowledge toward developing more effective sensors for monitoring pesticides and protecting public health.

Conflicts of interest

There are no conflicts to declare.

Data availability

The datasets generated and/or analyzed during this study are available from the corresponding author upon reasonable request. All experimental data, characterization results, and computational files supporting the findings of this work have been retained at the Indian Institute of Science, Bengaluru.

Supplementary information (SI) is available. See DOI: https://doi.org/10.1039/d5ra09371f.

Acknowledgements

References

1 A. Parven, I. M. Meftaul, K. Venkateswarlu and M. Megharaj, *Int. J. Environ. Sci. Technol.*, 2024, **22**(2), 1181–1202.

2 R. M. Ghazi, N. R. N. Yusoff, N. S. A. Halim, I. R. A. Wahab, N. Ab Latif, S. H. Hasmoni, M. A. A. Zaini and Z. A. Zakaria, *Bioengineered*, 2023, **14**(1), 1–21.

3 R. C. Gupta and P. K. Gupta, *Vet. Toxicol.*, 2025, 565–579.

4 K. Wang, Y. Ren, X. Pan, X. Wu, J. Xu, Y. Zheng and F. Dong, *J. Hazard. Mater.*, 2025, **490**, 137794.

5 S. Das, H. Sakr, I. Al-Huseini, R. Jetti, S. Al-Qasmi, R. Sugavasi and S. R. Sirasanagandla, *Plants*, 2023, **12**, 2278.

6 J. Bethsass and A. Colangelo, *Int. J. Occup. Environ. Health*, 2006, **12**, 260–267.

7 S. Datta, J. Singh, J. Singh, S. Singh and S. Singh, *Chemosphere*, 2021, **278**, 130476.

8 L. Y. Ma, N. Zhang, J. T. Liu, X. Y. Zhai, Y. Lv, F. F. Lu and H. Yang, *Environ. Int.*, 2019, **131**, 105014.

9 D. Arthur, Executive summary of safety and toxicity information atrazine, *National Toxicology Program*, Elsevier Ltd, 1992, vol. 276.

10 S. Singh, V. Kumar, D. S. Dhanjal, V. Dhaka, Sonali and J. Singh, in *Agricultural Biocatalysis: Theoretical Studies and Photosynthesis Aspects*, Pan Stanford Publishing Pte. Ltd., 2022, pp. 295–312.

11 K. Ralston-Hooper, J. Hardy, L. Hahn, H. Ochoa-Acuña, L. S. Lee, R. Mollenhauer and M. S. Sepúlveda, *Ecotoxicology*, 2009, **18**, 899–905.

12 P. Supraja, S. Tripathy, S. R. K. Vanjari, V. Singh and S. G. Singh, *Biosens. Bioelectron.*, 2019, **141**, 111441.

13 S. Singh, N. Pavithra, S. K. Behera, R. Varshney, J. Singh and P. C. Ramamurthy, *New J. Chem.*, 2024, **48**, 18836–18847.

14 S. Singh, N. Sivaram, B. Nath, N. A. Khan, J. Singh and P. C. Ramamurthy, *npj Clean Water*, 2024, **7**, 1–22.

15 W. Fan, K. Y. Wang, C. Welton, L. Feng, X. Wang, X. Liu, Y. Li, Z. Kang, H. C. Zhou, R. Wang and D. Sun, *Coord. Chem. Rev.*, 2023, **489**, 215175.

16 T. Wu, N. Prasetya and K. Li, *J. Membr. Sci.*, 2020, **615**, 118493.

17 A. Samokhvalov, *Coord. Chem. Rev.*, 2018, **374**, 236–253.

18 P. Narasimhappa and P. C. Ramamurthy, *Nanotechnol. Environ. Eng.*, 2025, **10**, 1–14.

19 T. Li, X. Ba, X. Wang, Z. Wang, J. Yang, Y. Cui and L. Wang, *Environ. Eng. Res.*, 2023, **28**, 1–9.

20 K. Barthelet, J. Marrot, G. Férey and D. Riou, *Chem. Commun.*, 2004, **4**, 520–521.

21 B. Seoane, V. Sebastián, C. Téllez and J. Coronas, *CrystEngComm*, 2013, **15**, 9483–9490.

22 K. Salem, B. R. Zarif, F. Hosseini and C. Karami, *Desalination Water Treat.*, 2024, **318**, 100393.

23 Y. Tan, Z. Sun, H. Meng, Y. Han, J. Wu, J. Xu, Y. Xu and X. Zhang, *Sep. Purif. Technol.*, 2019, **215**, 217–226.

24 I. H. Alsohaimi, *Sep. Purif. Technol.*, 2025, **357**, 130240.

25 A. E. J. Hoffman, L. Vanduyfhuys, I. Nevjestić, J. Wieme, S. M. J. Rogge, H. Depauw, P. Van Der Voort, H. Vrielinck and V. Van Speybroeck, *J. Phys. Chem. C*, 2018, **122**, 2734–2746.

26 F. T. Alshorifi, S. M. El Dafrawy and A. I. Ahmed, *ACS Omega*, 2022, **7**, 23421–23444.

27 T. Dutta, K. H. Kim, R. J. C. Brown, Y. H. Kim and D. Boukhvalov, *Sci. Rep.*, 2018, **8**(1), 5033.

28 J. Rafi, A. Rajan and B. Neppolian, *Electrochim. Acta*, 2023, **446**, 142079.

29 Q. Jin, M. Khandelwal and W. Kim, *Energy Storage Mater.*, 2024, **70**, 103464.

30 I. Senkovska, F. Hoffmann, M. Fröba, J. Getzschmann, W. Böhlmann and S. Kaskel, *Microporous Mesoporous Mater.*, 2009, **122**, 93–98.

31 S. Kim, K. Choi and S. Park, *Solid State Sci.*, 2016, **61**, 40–43.

32 F. Millange, C. Serre and G. Férey, *Chem. Commun.*, 2002, **2**, 822–823.

33 C. Li, L. Zhu, W. Yang, X. He, S. Zhao, X. Zhang, W. Tang, J. Wang, T. Yue and Z. Li, *J. Agric. Food Chem.*, 2019, **67**, 1277–1283.

34 Y. Duan, S. Qi, C. Lin, K. Chen and R. Zhou, *J. Energy Inst.*, 2025, **123**, 102246.

35 A. Najah, R. Jean-Marie-Desiree, D. Boivin, R. L. S. Canevesi, C. Noël, M. T. Izquierdo, A. Celzard, V. Fierro, L. De Poucques, G. Henrion and S. Cuynet, *Int. J. Hydrogen Energy*, 2024, **59**, 1014–1022.

36 X. Chen, X. Liu, L. Zhu, X. Tao and X. Wang, *Chemosphere*, 2022, **291**, 133032.

37 L. B. O. Dos Santos, G. Abate and J. C. Masini, *Talanta*, 2004, **62**, 667–674.

38 S. Singh, P. N., H. Kaur, R. Varshney, N. A. Khan, R. Kumar, A. K. Sharma, J. Singh and P. C. Ramamurthy, *Sci. Rep.*, 2024, **14**(1), 17662.

39 H. Moulahoum, *ACS Omega*, 2023, **8**, 41194–41203.

40 A. D. Silverman, U. Akova, K. K. Alam, M. C. Jewett and J. B. Lucks, *ACS Synth. Biol.*, 2020, **9**, 671–677.

41 C. Tortolini, P. Bollella, R. Antiochia, G. Favero and F. Mazzei, *Sens. Actuators, B*, 2016, **224**, 552–558.

42 S. Singh, P. N., R. Varshney, A. Panchal, P. C. Ramamurthy, J. Singh and N. Shehata, *Sci. Rep.*, 2025, **45024**, DOI: 10.1038/s41598-025-29632-9.

43 R. Liu, G. Guan, S. Wang and Z. Zhang, *Analyst*, 2010, **136**, 184–190.

44 S. Singh, P. N., R. Varshney, A. Panchal, N. Shehata, N. A. Khan, J. Singh and P. C. Ramamurthy, *Nanoscale Adv.*, 2025, **7**, 7273–7284.